Enhanced Anomaly Detection in Wire Ropes by Combining Structure and Appearance

Esther-Sabrina Wacker*, Joachim Denzler

Chair for Computer Vision, Friedrich Schiller University of Jena, 07737 Jena, Germany

Abstract

Automatic visual surface inspection is a challenging task, which has become important for quality assurance in the last years. Wire rope inspection is a special problem within this field. Usually, the huge and heavy ropes cannot be detached. Thus, an inspection of the ropes must be conducted, while the ropes are in use. The rope surface exhibits various appearance characteristics so that the existing, purely appearance-based approaches tend to fail.

We explicitly integrate information about the object geometry, which we obtain by aligning a sequence of 2d rope images with a perfectly regular 3d model of the rope. The rendering equation is used to link object geometry to the observed rope appearance. Based on the connection between geometry and surface appearance we build a probabilistic appearance model which serves as representation for normal surface variations. A robust localization of rope surface defects is achieved by means of anomaly detection. The presented approach has no need for knowledge about the illumination setting or the reflectance properties of the material.

An evaluation on real-world data from ropeways leads to an accuracy comparable to that of a human expert. With an accuracy of 95% and a false-alarm-rate of 1.5% the approach outperforms all other existing approaches.

Keywords: anomaly detection, image-based analysis, surface inspection

1. Introduction

During the past years, automatic approaches for visual surface inspection have become more and more important. In the majority of cases, texture analysis techniques are used to locate conspicuous or defective regions. The automatic *visual* inspection (AVI) of wire ropes is an important and even more challenging task. Damaged ropes pose a risk for the human life (*e.g* ropes used for elevators or ropeways). A manual inspection is often dangerous and very time-consuming. Usually, the huge and heavy ropes cannot be detached for inspection. Thus, camera systems were developed, which allow a digital acquisition of the whole rope circumference (Moll, 2003).

1.1. Challenges arising from an AVI of wire ropes

Anyhow, the acquisition with optical sensors leads to noisy images. Reasons for this are the highly reflective material of the ropes and contamination of the rope surface by *e.g* mud, oil or water. In both cases, this leads to image artifacts. In contrast, surface defects within the rope are usually small and inconspicuous. On this account, defects are hardly distinguishable from the natural variations. These circumstances turn the automatic detection of rope surface defects into a challenging problem, as one has to cope with a high intra-class variability and a poor inter-class separability. Two examples for typical rope defects are given in Figure 1. Figure 1(a) depicts the particular characteristics of broken wires. In the upper example, the gap between the wire ends is very small and the underlying layer of wires becomes visible. In such a case, the breaking edge is the most striking anomaly. The lower example shows a broken wire, which is missing almost within the complete, visible part of the strand. The two images in Fig-

*Corresponding author

Email addresses: esther.wacker@uni-jena.de (Esther-Sabrina Wacker), joachim.denzler@uni-jena.de (Joachim Denzler)

This manuscript is originally published in *Pattern Recognition Letters, Vol. 34, Issue 8, pp 942–953, 1 June 2013.*
The final publication is available at
http://www.sciencedirect.com/science/article/pii/S016786551300038X

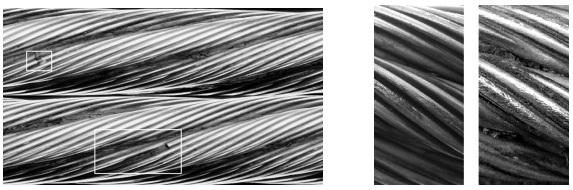

(a) broken wires (b) corrosion

Figure 1: Typical defects on the rope surface.

ure 1(b) illustrate the effect of surface corrosion. Due to mechanical forces, the surface material is damaged. Usually, such surface damages can be recognized best by their changed reflection behavior.

Additionally, a rope which oscillates during the acquisition procedure, leads to deformations in the images of the 2d rope sequence. This is due to the nature of the acquisition setup, where line cameras are used to record the rope. If the rope moves between two consecutive time steps, this results in a different spatial relation between rope and sensor. Hence, a combination of the individual 1d measurements into a 2d projection of the rope appears deformed.

However, the most striking challenge is the absence of defective training examples. Only few examples are available in advance. Due to the huge variety of defect characteristics it is nearly impossible to obtain a representative training set. In contrast, the number of examples for intact rope is exhaustless. Therefore, supervised classification approaches are not applicable to this problem domain. A solution for this problem is provided by the concept of *anomaly detection* (Chandola et al., 2009) which is strongly related to *one-class classification* (Tax, 2001). Anyhow, the performance of purely appearance-based approaches seems to be limited.

Last but not least, an automatic measurement of the rope would be of great interest for the purpose of rope inspection. To the best of our knowledge, such a monitoring of important rope parameters is not possible until today. Such parameters are *e.g* the lay lengths of wires and strands or the rope diameter. Usually, they underlie creeping changes and if the deviation from normality becomes to big, this is in general an evidence for problems within the rope formation which frequently are the cause for more severe rope defects.

1.2. Proposed Method

We present a model-based approach for visual surface inspection of wire ropes which is based on the principle of *analysis-by-synthesis*. The basic idea is to adapt a parametric 3d model towards reality by computing a

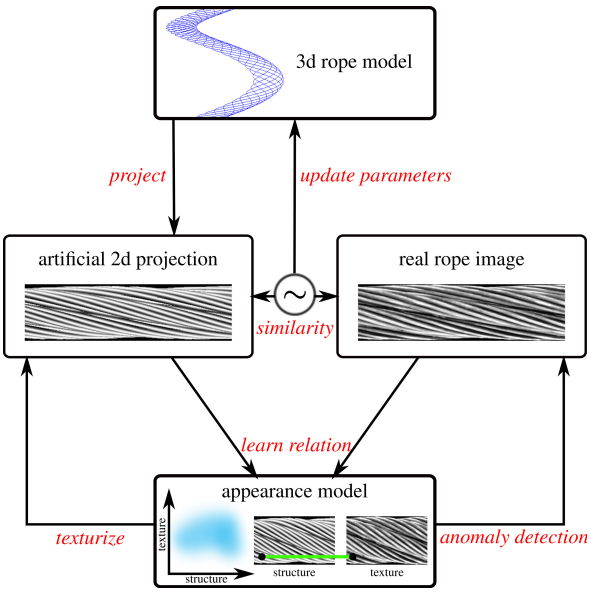

Figure 2: General framework used for the detection of surface defects in wire ropes.

2d projection of this model, which can be compared with the input image. We use this proceeding to compute a prediction of the intact rope surface in order to evaluate the discrepancy between the respective observation (real rope image) and the model-based forecast. Two different aspects contribute to the visual appearance of the rope: rope geometry (structure) and visual texture (appearance). Thereby, the term visual texture embraces all characteristic patterns of the rope surface (Tuceryan and Jain, 1998). Whereas the regular rope geometry forms the deterministic part, the visual texture with all its usual variations (reflections, mud, shadowing) is non-deterministic to a certain extent. Hence, it can be considered as random part more or less. Anyhow, there exists a dependence between visual texture and rope geometry, which we aim to learn from intact rope data.

Figure 2 gives an overview of our framework. The deterministic geometry of the rope can be modeled by a parametric 3d centerline model and we are able to compute artificial 2d projections of this model. The alignment of artificial rope model projections and real rope images results in a nonlinear optimization problem which leads to estimates for the free model parameters, which are the lay lengths of strands and wires. Based on the optimal parameters, the 2d wire course is predictable. This geometrical representation provides the possibility to infer the hidden relation between visual appearance and position within the rope. Thus, the im-

plicit relation between rope texture and rope geometry can be learned from a set of intact rope images. We use our knowledge about the rope geometry to sample the rendering equation (RE), which gives a physical explanation for the relation between object geometry and observed appearance. The periodic structure of the rope allows us to obtain several gray level measurements from the 2d rope sequence which correspond to the same 3d point in the rope model. By utilizing a probabilistically formulated appearance model, it becomes possible to cover all the usual appearance variations within the rope surface. Beyond that, the probabilistic treatment permits the direct derivation of an anomaly score on the pixel-level.

1.3. Contributions of this work

The advantages of our proceeding are obvious. Compared to purely appearance-based approaches, a combination of structure and appearance leads to a more sophisticated and accurate recognition of anomalies within the rope surface. Furthermore, the proposed approach allows for a continuous monitoring of the lay lengths of strands and wires along the whole rope course. Finally, the model-based proceeding allows for an easy correction of rope deformations in the images of the 2d rope sequence, which often hinder the recognition of defects within the rope. This oscillation correction, which we present in this work, clearly improves our previously published approach for rope geometry estimation (Wacker and Denzler, 2010). Once, the relation between structure and appearance is learned, every arbitrary deviation from normality should become recognizable. Our method is data-driven and purely image-based. Moreover, we have no need for calibration information with respect to camera positions or the illumination setting.

The remainder of this paper is structured as follows: in Section 2 we summarize previous and relevant work. Our proposed method for rope geometry estimation is introduced in Section 3. In Section 4, we focus on the hidden relation between rope geometry and visual texture. The defect detection methodology which makes use of the proposed statistical appearance model is described in Section 5. A comprehensive experimental evaluation, which leads to detection results comparable to those of a human expert, is presented in Section 6. A summary of our work and a discussion about further work conclude the paper.

2. Related Work

2.1. Automatic Visual Inspection

There exists a lot of work in the field of automatic visual inspection and defect detection in material surfaces. Good overviews over existing techniques are provided by Xie (2008) and Kumar (2008). Due to the wide field of application areas (fabric defect detection, surface analysis, rail inspection, crack detection etc.) most work focuses very specifically on the relevant problem domain. Among the statistical approaches, gray level statistics (Iivarinen, 2000; Chetverikov, 2000; Chetverikov and Hanbury, 2002), co-occurrence matrices (Rautkorpi and Iivarinen, 2005) and local binary patterns (Niskanen et al., 2001; Mäenpää et al., 2003; Tajeripour et al., 2008) are the most frequently used ones. Unser and Ade (1984) and Monadjemi et al. (2004) make use of an Eigenfilter approach. Common spectral methods are Gabor filters (Mandriota et al., 2001; Kumar and Pang, 2002), Fourier analysis (Chan and Pang, 2000) and wavelet-based approaches (Serdaroglu et al., 2006). Model-based approaches often model the stochastic variations of a surface with help of Markov random fields (Cohen et al., 1991). Due to the lack of defective training samples anomaly detection (Chandola et al., 2009; Markou and Singh, 2003a,b), one-class classification (Tax, 2001) and outlier detection (Hodge and Austin, 2004) are relevant concepts (Tajeripour et al., 2008; Xie, 2008).

2.2. Rope Inspection

There exists a lot of work in the field of automatic rope inspection by magnetic measurement techniques Zhang et al. (2006) but only few previous work coping with automatic approaches for *visual* rope inspection. Platzer et al. (2010) compared the performance of different textural features for the problem of defect detection in wire rope surfaces. In Platzer et al. (2009), they focused on contextual anomaly detection by modeling the intact class with help of Hidden Markov Models. Haase et al. (2010) analyzed contextual anomalies in the rope surface with help of an autoregressive model which predicts the intact surface appearance given its neighborhood. Rodner et al. (2011) used Gaussian processes in a one-class classification framework to detect anomalies in wire ropes. Nevertheless, none of these purely appearance-based approaches achieves the accuracy of a human inspector.

2.3. Analysis-by-Synthesis and Material Appearance Estimation

Analysis-by-synthesis (Koch, 1993) is a well-known approach for the problem of estimating time-variant

(dynamic) 3d scene parameters in an image-based manner. A parametric 3d model is adapted towards the real scene by synthesizing 2d model projections. The measurable differences between model and real image guide the model adaption within a feedback loop. Free model parameters correspond to the scene characteristics of interest such as *e.g* shape, position and surface reflectance. Where appropriate, the initial model estimation by computer vision algorithms comprises a fourth element (Koch, 1993). Typical application examples for analysis-by-synthesis include camera calibration (Eisert, 2002; Koeser et al., 2007; Wuest et al., 2007), human motion analysis (Moeslund et al., 2006) and (object) tracking applications (Hasler et al., 2007). A similar concept is used in medical applications for 2d-3d image registration with digitally reconstructed radiographs (DRR) (Penney et al., 1998).

If not only the scene geometry but also the surface appearance is of interest, image-based rendering (Shirley, 2002) aims to estimate the reflectance properties of material surfaces by optimizing the free parameters of the bidirectional reflectance distribution function (BRDF) in an image-based manner (Dana et al., 1999; Dana, 2001; Marschner et al., 2000). However, the estimation of the free model parameters requires a calibrated setup in which not only the object geometry but also all positions of the cameras and the light sources must be known.

In contrast, in this work we propose to neglect the term for reflectance in the parametric model description. Instead, a density model for the visual texture is directly learned from the image data based on the relation between rope geometry and observed surface appearance. Thus, it is possible to obtain an appearance model which also captures natural appearance variations which cannot be modeled with a parametric reflectance model due to their non-deterministic character.

3. Rope Geometry Estimation

To estimate the rope geometry from a 2d sequence of rope images, we follow the principle of analysis-by-synthesis. Instead of estimating the initial model from image data, we use our expert knowledge about rope construction to provide a mathematical formulation of the wire centerlines. This formulation serves as parametric rope model. The synthesis step comprises the computation of a 2d model projection according to the special projection geometry of the acquisition system. The model adaption is performed in hierarchical manner. First, the strands are aligned and deformations within the 2d rope images are corrected. Finally, the individual wires are aligned.

3.1. Parametric 3d Rope Model

A description of the general rope geometry can be found in Feyrer (2007). In order to keep the model simple, a wire centerline model is used instead of a volumetric one. A stranded rope consists of strands which are composed of wires. In the top left of Figure 3(a) the fundamental construction of a wire rope is shown: N strands (big circles) are grouped around the rope core (gray shaded) and each strand consists of M wires (small circles). A wire centerline $\boldsymbol{w}_{i,j}$ of the i-th wire in the j-th strand can be mathematically described by two intertwined helices (rotated around the y-axis to be aligned with the x-axis of the line camera coordinate system) dependent on the two parameter vectors $\boldsymbol{p}_s$ and $\boldsymbol{p}_{w_j}$.

$$\boldsymbol{w}_{i,j}(\boldsymbol{p}_s, \boldsymbol{p}_{w_j}, t) = \underbrace{\begin{pmatrix} t \\ r_s \sin(\varphi_s(\boldsymbol{p}_s, t)) \\ -r_s \cos(\varphi_s(\boldsymbol{p}_s, t)) \end{pmatrix}}_{\boldsymbol{s}_j} + \underbrace{\begin{pmatrix} 0 \\ r_w \sin(\varphi_w(\boldsymbol{p}_{w_j}, t)) \\ -r_w \cos(\varphi_w(\boldsymbol{p}_{w_j}, t)) \end{pmatrix}}_{\boldsymbol{w}_i}. \tag{1}$$

r_s and r_w are the radii of the strand and wire space curves. In detail, the phase angles can be formulated as a function of the parameter vectors $\boldsymbol{p}_s = \left(L_s, o_s\right)$ and $\boldsymbol{p}_{w_j} = \left(L_{w_j}, o_{w_j}\right)$:

$$\varphi_s(\boldsymbol{p}_s, t) = t\frac{2\pi}{L_s} + jk_s + o_s \tag{2}$$

$$\varphi_w(\boldsymbol{p}_{w_j}, t) = t\frac{2\pi}{L_{w_j}} + ik_w + o_{w_j}. \tag{3}$$

$jk_s = j\frac{2\pi}{N}$ and $ik_w = i\frac{2\pi}{M}$ denote the phase displacements for the j-th strand and the i-th wire respectively. L_s is the lay length of the individual strands whereas L_{w_j} denotes the wire lay length of the wires in strand j. o_s and o_{w_j} are the phase offsets and t is the current time step.

Note, that we refrain from using an additional index to indicate the strand and wire number on the phase functions φ_s and φ_w to increase the readability. The radii of the wire and strand space curves can be computed from the rope specification which contains the diameters of the strands and wires $\varnothing_s$ and $\varnothing_w$. Figure 3(a) shows that the wire space curve radius can be computed as $r_w = \frac{\sin(\beta)\varnothing_w}{\sin(\alpha)}$. The calculation of the strand curve radius is analog.

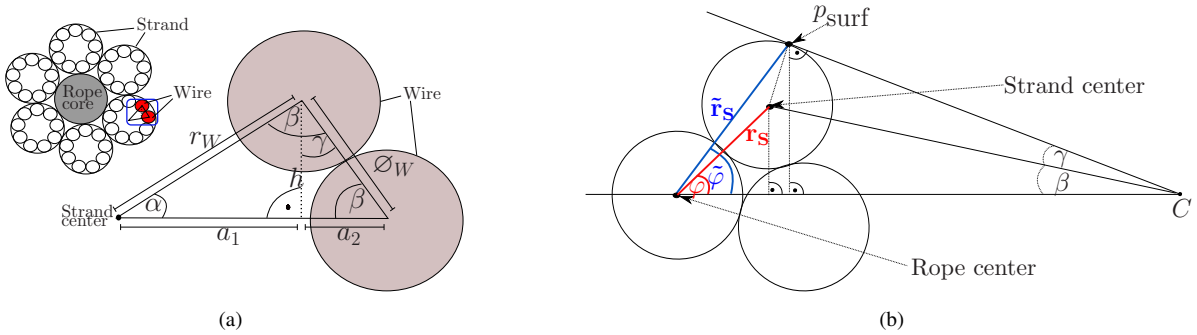

Figure 3: General rope and wire geometry (a) and geometry for the computation of the model contour of a volumetric rope projection (b).

3.2. Image Synthesis

For the image synthesis, the specific projection geometry of the camera system (Moll, 2003) must be taken into account. Four line cameras are placed equally around the rope and move with constant and linear motion along the rope axis during acquisition. The projection matrix for a so called *pushbroom camera* was derived by Gupta and Hartley (1997). We have to cope with a perspective projection along the sensor array and an orthographic projection along the time axis. According to Gupta and Hartley (1997) the pushbroom projection of a 3d rope point $\boldsymbol{w}_{i,j}(\boldsymbol{p}_s, \boldsymbol{p}_{w_j}, t)$ to a 2d point (u, v) can be written as:

$$\begin{pmatrix} u \\ v \end{pmatrix} \leftarrow \begin{pmatrix} u \\ wv \\ w \end{pmatrix} = \mathbf{K} \cdot \mathbf{V} \left(\boldsymbol{w}_{i,j}(\boldsymbol{p}_s, \boldsymbol{p}_{w_j}, t) + \begin{pmatrix} 0 \\ 0 \\ d \end{pmatrix} \right). \quad (4)$$

The camera-to-scene distance d is unknown. The intrinsic camera parameters $\mathbf{K}$ are also unknown but fixed. However, the 3d rope diameter $\varnothing_r$ as well as the rope diameter in pixels in the real 2d projection $\varnothing_r^{2d}$ are known. Hence, we set the focal length $f = 1$ and the projection center $p_v = 0$ and rescale the resulting projection to the known rope diameter in pixels. An optimization of d conjointly with the other free parameters leads to an estimation of the ratio between f and d. Matrix $\mathbf{V}$ includes the camera movement and degenerates to an identity matrix in our special case of constant camera movement along the x-axis. The projection of a 3d rope point $\boldsymbol{w}_{i,j}(\boldsymbol{p}_s, \boldsymbol{p}_{w_j}, t)$ in Cartesian coordinates results from (1) and (4):

$$\begin{pmatrix} u, & v \end{pmatrix}^T = \left(t, \quad \frac{r_s \sin(\varphi_s(\boldsymbol{p}_s,t)) + r_w \sin(\varphi_{w_j}(\boldsymbol{p}_{w_j},t))}{-(r_s \cos(\varphi_s(\boldsymbol{p}_s,t)) + r_w \cos(\varphi_{w_j}(\boldsymbol{p}_{w_j},t))) + d} \right)^T. \quad (5)$$

As a centerline model is used, the volumetric wire appearance must be approximated to simplify the alignment procedure. For this purpose, a 1d Gaussian is centered around each projected wire centerline pixel with a mask width corresponding to the projected wire diameter in pixel. Although only heuristically motivated, a Gaussian approximates the illumination properties around the wires sufficiently.

3.3. Rope Parameter Optimization

The alignment of the artificial projections with the real rope images results in estimates for the free rope parameters. The image registration is performed within a non-linear optimization framework. Free model parameters are the lay lengths of strands and wires as well as the strand and wire positions. Furthermore, the camera-to-scene distance must be estimated for the first view of a sequence, in order to obtain a correct scaling of the artificial projections. As the distance between camera and rope remains more or less equal during the acquisition process, all further processing can be based on this estimate. The alignment of periodic structures always results in an ambiguous registration problem. This problem is exacerbated by the fact that the wire parameters are highly dependent on the strand parameters. We take advantage of the hierarchical design of a stranded rope to simplify this problem. At first, solely the strands are aligned. For this purpose, we provide an analytic description of the rope contours. The analytic treatment allows for the usage of efficient similarity measures. Apart from this, the image deformations which arise from an oscillating rope during acquisition can be simultaneously corrected by estimating the displacement of real rope contour and model contour. Finally, the wires of each individual strand can be aligned separately in image-based manner. The wire alignment closes the analysis-by-synthesis loop.

3.3.1. Strand Alignment and Deformation Correction

The alignment of the real rope contours and the projected model contours results also in an alignment of the

strands. Therefore, the upper and lower rope contours $rc^u(t)$ and $rc^l(t)$ can be extracted automatically from the real rope images. The iterative optimization strategy is composed of the following steps, which will be described in detail afterwards:

(1) Derive analytic description of upper and lower model contours $mc^u(\boldsymbol{p}_s, t)$ and $mc^l(\boldsymbol{p}_s, t)$ for current parameter setting $\boldsymbol{p}_s$
(2) Computation of the displacement vector $\hat{\boldsymbol{y}}^{\boldsymbol{p}_s}$ of real and synthetic contours (pixel coordinates)
(3) Correction of the real contour by $\hat{\boldsymbol{y}}^{\boldsymbol{p}_s}$
(4) Computation of the normalized 1d cross correlation coefficient $NCC_T^{1d}[\cdot,\cdot]$ of both contours

(1) *Model Contours.* The analytic description of the projected model contours is based on the geometric relations between a point on the strand center line and a point on the strand surface which is a part of the model rope contour, which are illustrated in Figure 3(b). The strand center which results in a contour point in the 2d *centerline* projection can be described by the angle φ_s and the radius of the strand space curve r_s (both marked in red). However, to describe the 3d point p_{surf}, which results in a contour point of the *volumetric* 2d rope projection, a new angle $\tilde{\varphi}_s$ and a new distance $\tilde{r}_s$ (marked in blue) can be computed with help of trigonometric operations. Thus, the contour of the volumetric 2d model projection of a strand $\tilde{\boldsymbol{s}}_j^{2d}$ can be described by:

$$\tilde{\boldsymbol{s}}_j^{2d}(\boldsymbol{p}_s, t) = \begin{pmatrix} t \\ \frac{\tilde{r}_s \sin(\tilde{\varphi}_s(\boldsymbol{p}_s,t))}{-(\tilde{r}_s \cos(\tilde{\varphi}_s(\boldsymbol{p}_s,t)))+d} \end{pmatrix}. \tag{6}$$

Consequently, the contour of the whole rope in the volumetric 2d rope projection in image coordinates can be simply derived by a minimum/maximum operation on the v-coordinates $\tilde{s}v_j^{2d}$ of (6) for all strands in one *time frame* $T = [t_1, t_n]$:

$$mc^l(\boldsymbol{p}_s, t) = \min_j \tilde{s}v_j^{2d}(\boldsymbol{p}_s, t), \quad \forall t \in T \tag{7}$$

$$mc^u(\boldsymbol{p}_s, t) = \max_j \tilde{s}v_j^{2d}(\boldsymbol{p}_s, t), \quad \forall t \in T. \tag{8}$$

(2) *Displacement Vector.* It is possible to rescale the model contour to pixel coordinates with help of the pixel ranges obtained from the real contour. Afterwards, the correction vector $\boldsymbol{y}^{\boldsymbol{p}_s} = (y_{t_1}^{\boldsymbol{p}_s}, \ldots, y_{t_n}^{\boldsymbol{p}_s})$ for the given time frame $T = [t_1, t_n]$ and the current parameter set $\boldsymbol{p}_s$ can be computed by the concept of least squares:

$$\hat{\boldsymbol{y}}^{\boldsymbol{p}_s} = \arg\min_{\boldsymbol{y}^{\boldsymbol{p}_s}} \sum_{t=t_1}^{t_n} \left(\left(rc^u(t) + y_t^{\boldsymbol{p}_s}\right) - mc^u(\boldsymbol{p}_s, t)\right)^2 + \left(\left(rc^l(t) + y_t^{\boldsymbol{p}_s}\right) - mc^l(\boldsymbol{p}_s, t)\right)^2. \tag{9}$$

Solving for $\hat{y}_t^{\boldsymbol{p}_s}$ for all $t \in T$ leads to:

$$\hat{y}_t^{\boldsymbol{p}_s} = 0.5\ (mc^u(\boldsymbol{p}_s, t) - rc^u(t) + mc^l(\boldsymbol{p}_s, t) - rc^l(t)). \tag{10}$$

Although least squares is known to be prone to outliers, this is not a problem for the following step. The correlation coefficient which is maximized for the alignment of the model contours and the real contours (step 4) is computed with respect to a whole time frame which provides the necessary context to cope with outliers.

(3) *Contour Correction.* The original rope contours are corrected by the estimated deformation vector $\hat{\boldsymbol{y}}^{\boldsymbol{p}_s}$ as follows

$$rc^u(t)' = rc^u(t) + \hat{y}_t^{\boldsymbol{p}_s}, \tag{11}$$

$$rc^l(t)' = rc^l(t) + \hat{y}_t^{\boldsymbol{p}_s} \tag{12}$$

for all $t \in T$. Furthermore, the deformation vector, which is estimated for the final strand parameters in the last optimization iteration, must be applied to the whole rope projection, in order to ensure a robust wire alignment.

(4) *Correlation Coefficient.* For the optimization of $\boldsymbol{p}_s$ the 1d cross correlation coefficient $NCC_T^{1d}[\cdot,\cdot]$ of the model contours and the corrected real rope contours is maximized:

$$\hat{\boldsymbol{p}}_s = \arg\max_{\boldsymbol{p}_s} (NCC_T^{1d}\left[rc^u(t)', mc^u(\boldsymbol{p}_s, t)\right] + NCC_T^{1d}\left[rc^l(t)', mc^l(\boldsymbol{p}_s, t)\right]). \tag{13}$$

3.3.2. Wire Alignment

Based on the strand alignment the alignment of wires is done separately for each individual strand. Consequently, the wires of different strands possess an individual parameter set (which is analog to the making of a real rope). The alignment task turns out to be a multimodal registration problem of the artificial projection with the real rope image. Hence, similarity measures like the (weighted) mutual information and the 2d normalized correlation coefficient are perfectly suited and work well for our problem formulation. For the sake of simplicity, we formulate the alignment of the synthetic projection $\mathcal{I}_m$ with the real projection $\mathcal{I}_r$ and time frame T using the normalized correlation coefficient $NCC_T^{2d}[\cdot,\cdot]$ only:

$$\hat{\boldsymbol{p}}_{w_j} = \arg\max_{\boldsymbol{p}_{w_j}} NCC_T^{2d}\left[\mathcal{I}_r, \mathcal{I}_m(\hat{\boldsymbol{p}}_s, \boldsymbol{p}_{w_j}, t)\right]. \tag{14}$$

For the optimization of both, strands and wires, we use the Downhill Simplex optimization scheme (Press

et al., 1992). Prior to the Downhill Simplex we furthermore perform a global grid search. This is done because the wire alignment is highly periodic. Hence, this ambiguous optimization problem requires a good initialization.

4. Combination of Structure and Appearance

This section describes, how we can learn the implicit relation between rope texture and rope geometry from a set of intact rope images. As already mentioned, our rope model representation neglects a parametric reflectance model. Nevertheless, there exists a physical explanation for the relation between object geometry and observed appearance, which is briefly introduced in Section 4.1. We show that the periodically repeating rope geometry and the special and fixed spatial relationship between rope, light source and camera allow for a sampling of this physical model which is known as *rendering equation* (RE). This sampling results in our probabilistic appearance model. In contrast to a parametric reflectance model this approach is able to capture all normal variations within the surface characteristics even if they are of non-determinstic nature.

4.1. Physical Model for Appearance

The rendering equation is an integral equation describing the propagation of light. It was first introduced by Kajiya (1986) and gives a physical explanation for the radiance, which can be observed at a surface point $\boldsymbol{X}$ of an object dependent on the viewing direction $\boldsymbol{\omega}_o$.

$$L_O(\boldsymbol{X}, \boldsymbol{\omega}_o) = \tag{15}$$
$$L_E(\boldsymbol{X}, \boldsymbol{\omega}_o) + \int_\Omega f_r(\boldsymbol{X}, \boldsymbol{\omega}_i, \boldsymbol{\omega}_o)\, L_I(\boldsymbol{X}, \boldsymbol{\omega}_i)\, (\boldsymbol{\omega}_i \cdot \boldsymbol{n}) d\boldsymbol{\omega}_i.$$

The outcome L_O is influenced by the emitted amount of light L_E and the reflected amount of light. The reflected radiance is the product of the incoming radiance L_I, the bidirectional reflectance distribution function f_r of the surface point and the inner product of surface normal $\boldsymbol{n}$ and the inward direction $\boldsymbol{\omega}_i$ integrated over the hemisphere Ω. For non-emitting surfaces, the self-emission L_E can be neglected.

Usually, an analytical solution of the rendering equation is not possible. Therefore, it is approximated with help of simpler, but often not physically correct illumination models like *e.g* the Phong shading (Phong, 1975). Or it is sampled with help of Monte Carlo techniques like path tracing or photon mapping (Lafortune, 1996; Jensen, 2001). Nevertheless, all of these approximations require knowledge about the position of the light sources as well as the viewing angle.

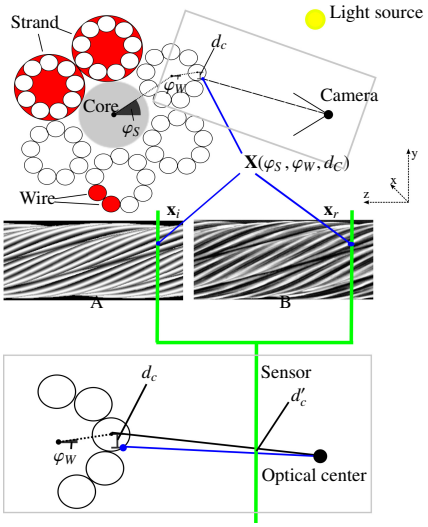

Figure 4: Scenario sketch: given the point correspondence of a rope pixel $\boldsymbol{x}_r$ in the real rope image (B) and a rope pixel $\boldsymbol{x}_i$ in the aligned artificial model projection (A) a 3d surface point $\boldsymbol{X}$ of the rope can be parametrized by the two phase angles φ_s, φ_w and the 2d distance d'_c of $\boldsymbol{x}_i$ to its corresponding projected wire centerline. d'_c results from a 1:1 mapping of the unknown 3d distance d_c.

4.2. Geometry-dependent Appearance Sampling

As the visual inspection of wire ropes cannot be performed within a controlled environment it is a hard task to provide adequate calibration information with respect to the acquisition setup in order to estimate the RE with common techniques. This basically implies, that $\boldsymbol{\omega}_o$ and $\boldsymbol{\omega}_i$ of (15) are unknown. However, the relation between camera, object, and position of the light source(s) stays fixed. The camera system used for the rope acquisition is closed and therefore minimizes the influence of the natural illumination (*e.g* sun light). For this case, it is obvious that the viewing direction as well as the incident angle of the incoming light depend only on the surface point $\boldsymbol{X}$. Figure 4 clarifies this circumstance. Given the aligned real rope images and the artificial model projections we obtain a correspondence between a pixel $\boldsymbol{x}_i$ in the artificial projection and a pixel $\boldsymbol{x}_r$ in the real image. Thus, it is also possible to derive a parametric description of the surface point $\boldsymbol{X}$ which is fully described by the two phase angles φ_s and φ_w and the appropriate 3d distance d_c of this surface point $\boldsymbol{X}$ to the visual line which crosses the corresponding wire centerline (time

is neglected):

$$\boldsymbol{X}(\varphi_s(\boldsymbol{p}_s), \varphi_w(\boldsymbol{p}_{w_j}), d_c) = \boldsymbol{w}_{i,j}(\boldsymbol{p}_s, \boldsymbol{p}_{w_j}) + \underbrace{\begin{pmatrix} 0 \\ d_c \\ -\sqrt{0.5\varnothing_w^2 - d_c^2} \end{pmatrix}}_{\boldsymbol{n}'}. \tag{16}$$

The vector $\boldsymbol{n}'$ points into the direction of the surface normal. Although d_c is unknown due to the missing volumetric information there exists a 1:1 mapping between d_c and the measurable 2d distance d_c' of an image pixel $\boldsymbol{x}_i$ to its corresponding projected wire centerline. Thus, we replace the unknown distance d_c by is measurable counterpart d_c'. Hence, each surface point can be uniquely adressed by its parametric description $\boldsymbol{\theta} = (\varphi_s(\boldsymbol{p}_s), \varphi_w(\boldsymbol{p}_{w_j}), d_c')$.

Based on this description, we can re-parametrize (15)

$$\tilde{L}_O(\boldsymbol{\theta}) = L_O(\boldsymbol{X}(\boldsymbol{\theta})) = \int_\Omega f_r(\boldsymbol{X}(\boldsymbol{\theta}), \boldsymbol{\omega}_i)\; L_I(\boldsymbol{X}(\boldsymbol{\theta}), \boldsymbol{\omega}_i)(\boldsymbol{\omega}_i \cdot \boldsymbol{n}(\boldsymbol{X}(\boldsymbol{\theta})))d\boldsymbol{\omega}_i. \tag{17}$$

The emitting term L_E can be neglected as the rope is a non-emitting object. This re-parametrization allows for a sampling of the rendering equation dependent on the parametrization $\boldsymbol{\theta}$ of a surface point $\boldsymbol{X}$. Due to the periodicity of the rope which results in repeated samples for the same surface point, this allows us to estimate a density model for the relation between rope geometry and observed appearance. The appearance representation is formed by estimating the joint distribution $p(g_r, \boldsymbol{\theta})$ for any surface point parametrization $\boldsymbol{\theta}$ and the corresponding observed gray values g_r in the rope image. The density is estimated in a non-parametric manner with help of a 4d histogram and we obtain a dense representation by applying a 4d Parzen estimator:

$$p(z = (g_r, \boldsymbol{\theta})) = \frac{1}{n}\sum_{i=1}^{b} \frac{1}{\sqrt{|2\pi\boldsymbol{\Sigma}|}} \exp\left(-\frac{1}{2}(z - z_i)^T\, \boldsymbol{\Sigma}^{-1}\, (z - z_i)\right) n_i. \tag{18}$$

n denotes the total number of all available samples whereas n_i is the number of samples belonging to the histogram bin i. b is the total number of bins in the multidimensional histogram. The covariance matrix

$$\boldsymbol{\Sigma} = \begin{pmatrix} \sigma_1^2 & 0 & 0 & 0 \\ 0 & \sigma_2^2 & 0 & 0 \\ 0 & 0 & \sigma_3^2 & 0 \\ 0 & 0 & 0 & \sigma_4^2 \end{pmatrix} \tag{19}$$

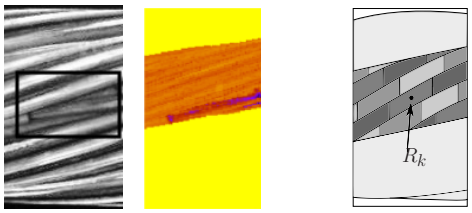

(a) (b)

Figure 5: (a): Original rope image with defect (left) and corresponding probability map (right). (b): Sketch of the rope regions.

defines the Gaussian window and $\sigma_1, \ldots, \sigma_4$ where chosen manually and are oriented towards the different variances along the histogram dimensions. As the real rope images have a gray level range of 256 values while the distances of the individual pixel $\boldsymbol{x}_i$ to its corresponding wire centerlines in synthesized model projections have a much smaller range, also the quantization of the real gray values was chosen to be coarser than that of the model domain.

The estimated density combines rope structure and observed surface appearance and results in a generative model for the rope surface characteristics.

5. Rope Surface Analysis

Detecting defects in the rope surface means to discover anomalous regions in the image. Therefore, the defect diagnosis can be treated as an anomaly detection problem. The rope model is aligned with the query image and this results in a parametrization $\boldsymbol{\theta}$ for each surface point corresponding to a rope pixel in the query image. A probability map is computed with help of the likelihood

$$p(g_r \mid \boldsymbol{\theta}) = \frac{p(g_r, \boldsymbol{\theta})}{p(\boldsymbol{\theta})}. \tag{20}$$

(20) states how likely it is to observe the gray value g_r for a pixel $\boldsymbol{x}_r$ given its corresponding parametrization $\boldsymbol{\theta}$. This likelihood can be extracted from the appearance representation $p(g_r, \boldsymbol{\theta})$ introduced in Section 4.2. In the left of Figure 5(a), a rope image including a typical defect is shown. The appropriate probability map is depicted in the right of Figure 5(a). The darker the color in the probability map, the smaller the obtained likelihood.

Nevertheless, an alignment of a rigid rope model with the flexible structure of a real rope leads to systematic registration inaccuracies, which arise mainly in the border areas between two strands. In these regions, a robust estimation of the appearance model is hindered and the estimated density becomes broad. For this reason, the

appearance model needs to be normalized with respect to these registration inaccuracies.

With help of the two phase angles φ_s, φ_w the rope surface can be divided into several clusters or regions. This is sketched in Figure 5(b). The rope surface is separated into K discrete region classes R_k and the expectation of each individual rope region is normalized. This is done by computing the average likelihood $\overline{p}(R_k)$ for each rope region R_k and all N_k rope pixels belonging to R_k:

$$\overline{p}(R_k) = \frac{1}{N_k} \sum_{n=1}^{N_k} p(g_r^n \mid \boldsymbol{\theta}^n) \ . \tag{21}$$

This average is now used to obtain a normalized likelihood according to (20):

$$\tilde{p}(g_r \mid \boldsymbol{\theta}) = p(g_r \mid \boldsymbol{\theta}) \ \frac{1}{\epsilon + \overline{p}(R_k)} \ . \tag{22}$$

In this case, $\epsilon > 0$ is a stabilization factor. The normalization is data-independent and can be performed on the training set, as it compensates for a systematic problem caused by the rigid nature of the rope model. To localize anomalies in the rope surface the normalized probability map including all normalized likelihoods $\tilde{p}(g_r \mid \boldsymbol{\theta})$ is mean filtered along the wire course. By applying a thresholding operation a hard assignment can be made, which differentiates between normal surface characteristics and suspicious changes in the rope surface. The threshold will be evaluated in detail in Section 6.

6. Experimental Evaluation

The approach and all important intermediate steps are evaluated thoroughly on real-world data which was acquired by the system described in Moll (2003). This line camera system delivers four individual views of the rope. Thus, the amount of rope meters is quadrupled and the set of natural variations which occur during the acquisition process is augmented. The camera system provides a temporal resolution of 0.1 mm per camera line. After a brief description of the different data sets and our evaluation criteria, the alignment accuracy is evaluated in Section 6.3. The most important results are provided in Section 6.4 where our approach is used to perform an automatic visual rope inspection in order to detect defects on the rope surface. For the sake of completeness we also prove that our generative model can be used to synthesize naturally appearing rope. Finally, we compare the defect detection performance with the results of another state-of-the art approach for automatic visual rope inspection. Note, that this purely appearance-based approach does not allow for an estimation of the rope geometry. As to the best of our knowledge, the presented approach is the first one which facilitates an automatic monitoring of the rope structure, we are not able to compare our results to other approaches with respect to the alignment accuracy.

6.1. Data sets

The anomaly detection accuracy is evaluated on real-world data acquired from an rope during operation. This data set, which we refer to with `RealRope`, comprises in total 7.7 GB. Note, that this corresponds in total to $4 \times 400\,\text{m} = 1600\,\text{m}$ of rope. The rope diameter is 32.0 mm and the expected average strand lay length (which results from the construction type) is 220.0 mm. Note, that a deviation of the lay length by a few mm is normal due to manufacturing variations. The data was carefully selected by a human expert to ensure, that a maximum amount of appearance variations and surface defects are contained. The reference labeling, which we consider as the gold standard, is also provided by the human expert. Note, that the labeling results of different experts differ not significantly. Thus, our labeling corresponds the results of a human inspector with respect to one in-depth inspection run. Altogether, there are 37 different surface defects in the rope. Some of them are visible in more than one camera view.

Anyhow, it is not possible to evaluate the alignment accuracy on real-world rope data in quantitative manner. This is due to the fact that it is not possible to measure an attached rope manually during operation. To provide a quantitative evaluation of the alignment accuracy we use an artificial reference data set `ArtificialRope`. It is worth noting, that although this reference data is computed based on the 3d rope model, the extraction of the rope contour from the real data is a critical part of the analysis and forms the foundation for the parameter estimation task. The synthetic rope is composed of six strands and nine wires. For each individual test run we simulate 30 m rope. The temporal resolution is 0.1 mm per camera line. The ground truth values of all free parameters for every individual test run are randomly chosen with strand lay lengths altering from 123 mm to 152 mm and wire lay lengths from 59 mm to 99 mm. To evaluate the accuracy of the presented approach Gaussian noise with different noise levels is added to the rope contours and the gray values of the resulting artificial rope projections.

To prove the general applicability of the approach on real rope data, we acquired a very short rope (3.4 meters) within a controlled environment. This facilitates a manual measurement of the lay lengths of strands and wires for small parts of this rope by a human expert.

The acquired rope has a diameter of 20.46 mm, and an expected strand lay length of 137.5 mm. We refer to this data set with `ShortRope`. To prove, that our approach is able to capture changes with respect to the lay lengths, we recorded three different sequences of the rope. **Seq.1** is the reference sequence. For **Seq.3** the rope was manually untwisted and for **Seq.2** is was retwisted. These manipulations should primarily result in an altered strand lay length. It is important to mention, that this rope contains no defects at all. Thus, it is not suitable for an evaluation of the defect detection performance and was acquired explicitly for the evaluation of the parameter monitoring accuracy.

6.2. Evaluation Criteria

The evaluation criteria which are applied to judge the alignment accuracy, the deformation correction and the anomaly detection performance are different. With respect to the alignment accuracy, the quality of the estimates for the strand lay length and the wire lay length are of interest. These are the important rope variables, as a strong variation with respect to these parameters gives evidence of severe problems within the rope formation. An evaluation on `ArtificialRope` allows for the computation of metric errors for these parameter estimates. Furthermore, for `ShortRope` it is possible to compare our parameter estimates to those resulting from the manual measurement. Anyhow, for real-world rope data it is only possible to provide a qualitative analysis as no ground truth information for the rope parameters is available. For this purpose, we display the real rope and the projected model strands and wires for the optimal parameter set in alternating fashion.

With respect to the deformation correction we face a similar problem. As it is not possible to determine the movement of the rope during acquisition, there exists no ground truth information. For this reason, we first provide a qualitative analysis to show the benefit for the overall alignment accuracy, which results from this correction step. To provide also a quantitative evaluation as proof-of-concept, we first compute the correction vector $\hat{\boldsymbol{y}}^{\boldsymbol{p}_s}$ for the images contained in `RealRope`. Next, we additionally apply a known distortion to the 2d rope sequence and recompute the correction vector for the individual frames. Now, given the two different correction vectors we are able to compute the root mean square error (rms) with respect to the artificial image transformation.

The anomaly detection problem can be considered as binary classification problem. According to Provost et al. (1998) the evaluation of binary classification systems by accuracy or recognition rates can be misleading. Thus we use receiver operating characteristic (ROC) curves and the corresponding area under the curve (AUC) measure to evaluate our approach. Note, that we treat a defect as positive test outcome and thus the true positive rate (TPR) determines the amount of recovered defect area measured in camera lines. In consequence, the false positive rate (FPR) measures the amount of false-alarms. Anyhow, it is not sufficient to measure the error just as a function of the total length of detected anomalies. This is due to the reason, that it is crucial to detect *every* single defect within the rope. Therefore, we introduce the 50% recovery case and mark that point of the ROC curve with a black square, which corresponds to the recognition rates, which can be achieved if at least 50% of the defect area are recognized. It is important to highlight, that these rates are bounded to the most challenging defects within the sequence. For the application it is not important to recover exactly 100% of the defect area but if significantly less then 50% of an anomaly are recovered, it is not clear whether this detection is a lucky shot.

6.3. Alignment Accuracy

The following experiments were designed to reveal the alignment accuracy of the 3d rope model with the 2d real rope images.

6.3.1. Quantitative Evaluation on Simulated Data

The quantitative evaluation of the alignment accuracy is performed on `ArtificialRope`. For both, the strand lay length estimates as well as the wire lay length estimates, we computed the metric estimation errors. The resulting error distributions are visualized by means of box plots (McGill et al., 1978). In Figure 6 the boxes depict the 0.25 and 0.75 quantiles and the middle bar marks the median error in millimeters obtained for all time steps of 20 randomly initialized test runs per noise level. Figure 6(a) shows the results for the strand parameter L_s and Figure 6(b) illustrates the error distribution for the wire lay length L_{w_j} of an exemplary chosen strand. The maximum position errors are around 1.3 mm and the camera-to-scene distance d can be measured with a mean accuracy of approximately 3.7 mm. Although this high accuracy is obtained with respect to a simulated test data set, these results prove the functional capability of our approach.

In order to prove the capability of the approach to track parameter variations, a randomly generated parameter progression is precomputed for every individual lay length parameter. This progression is marked by the gray area in Figure 6(c) and Figure 6(d). The estimates

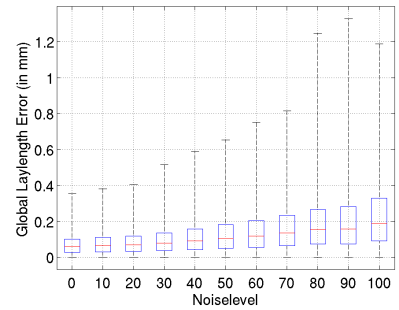

(a) Strand lay length estimate.

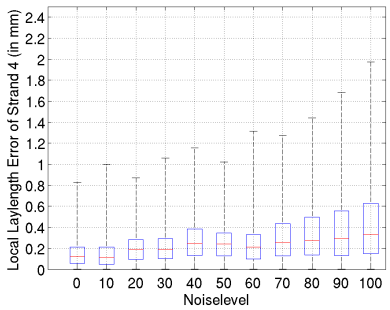

(b) Wire lay length estimate.

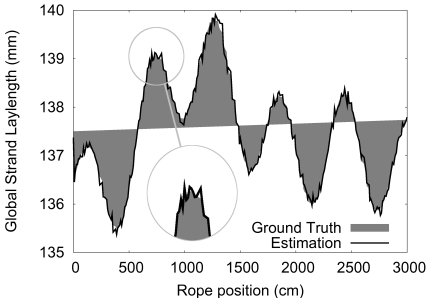

(c) Parameter tracking of lay lengths for strands.

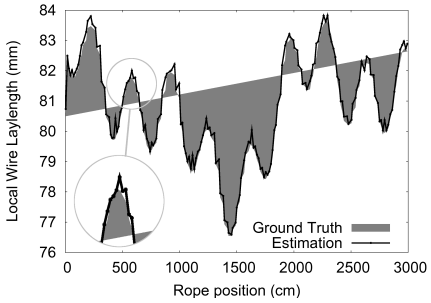

(d) Parameter tracking of lay lengths for wires.

Figure 6: (a)-(b): Robustness of the lay length estimates to noise. (c)-(d): Parameter tracking results. The gray area represents the ground truth parameter progression, the black curve corresponds to the estimates.

for every frame resulting from the analysis-by-synthesis loop are represented by the solid, black curve. The high accuracy is also reflected in the low mean errors obtained in 100 randomly initialized test runs. These are 0.06 mm for the strand lay length and 0.23 mm for the wire lay lengths.

6.3.2. *Results on Real Rope Data within a Controlled Environment*

We performed a model alignment for all three sequences of `ShortRope`. The parameter tracking results for the strand lay length of the three different sequences are displayed in Figure 7. The manually measured strand reference lay length for some exemplary frames of each sequence is given by the dashed line. This value is 136.6 mm for **Seq.1**, 139.5 mm for **Seq.2** and 133.0 mm for **Seq.3**. From Figure 7 it becomes clear that our estimated lay length matches the measurement of the human expert (dashed lines) for each of the three sequences. The variation in the estimation results varies over time around ± 1 mm which is less then one percent of the measured value. These are good results given the fact that the lay length is a time-variant, dynamic parameter and a reference is hardly to define by

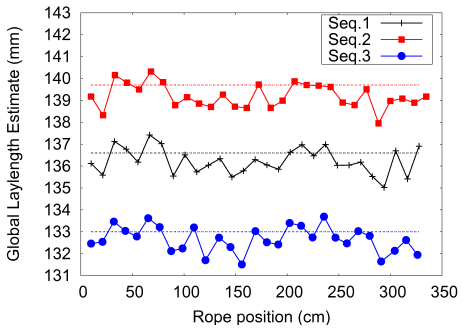

Figure 7: Strand lay length estimation on the three different real data sequences.

manual measurement. Furthermore, we would like to draw the reader's attention to the visible correlation in the lay length course of the three different sequences. Bearing in mind, that all sequences are acquired from the same rope, this is a further indicator for the quality of our estimation results. The variation coefficient (standard deviation/mean) for 10 different estimation runs is 0.0028% for the strand lay length and 3.3% for the wire lay lengths.

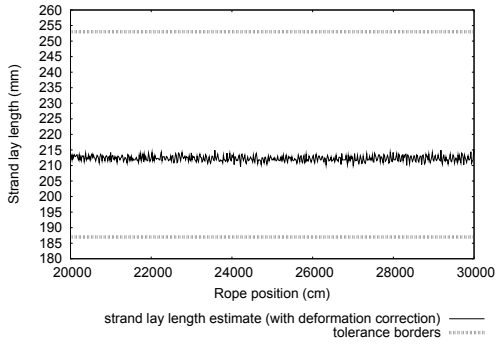

(a) Strand lay length estimation.

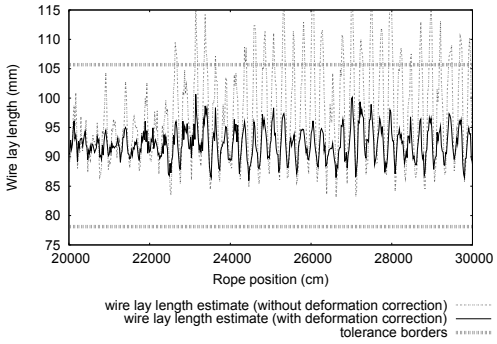

(b) Wire lay length estimation with and without deformation correction.

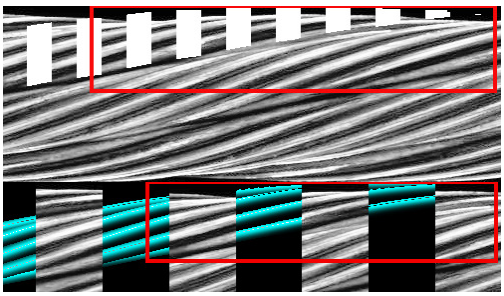

(c) Alignment without deformation correction.

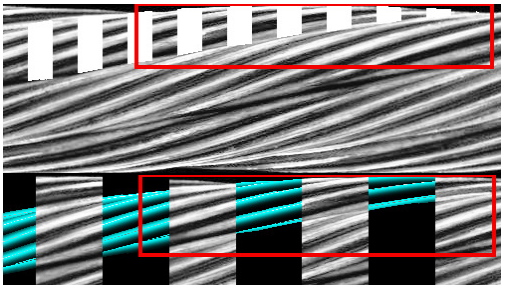

(d) Alignment with deformation correction.

Figure 8: (a)-(b): Lay length estimation on a representative part of the real rope. (c)-(d): Influence of the deformation correction on the alignment result with wire lay length estimates given in brackets. The first image (c) shows the result without deformation correction (107.15 mm). In the top the strand back projection is shown. In the bottom, the wire alignment is displayed. The second image (d) shows the same result but with deformation correction (95,32 mm)

6.3.3. Qualitative Evaluation on Real-World Rope Data

Figure 8(a) shows the parameter tracking result for the strand lay lengths obtained on the data set `RealRope`. For a better readability of the plot, just the results for a representative part of the rope are displayed. The dotted lines mark the upper and lower tolerances for the lay length, defined by the human expert given the theoretic lay length for this rope construction type. The parameter estimation results are robust and vary in between 3% of the expected lay length. Obviously, this rope seems not to suffer from creeping changes with respect to its geometric structure.

Figure 8(b) shows the parameter tracking result for the wire lay length of one exemplary chosen strand of `RealRope` with deformation correction and without deformation correction. The deformation correction clearly leads to more robust estimates of the wire lay length. Note, that small imprecisions with respect to the strand parameter estimates will change the outcome of the wire parameter estimates. However, this must not necessarily imply a wrong wire alignment, as small inaccuracies with respect to the strand parameter estimates can be balanced by lightly modified wire parameter estimates. The qualitative analysis of the wire alignment and the deformation correction is given in Figure 8(c) and Figure 8(d). The top row of both images depicts the strand backprojection of the model strand into the real rope image and the bottom row shows the wire backprojection respectively. The images on the left hand side (8(c)) show the alignment result without an additional deformation correction and the right hand size (8(d)) illustrates the results obtained with deformation correction. Obviously, the deformation correction improves the alignment results significantly, especially with regard to the marked regions of interest.

Finally, the mean rms with respect to 100 randomly generated deformation vectors, which were additionally applied to the image data from randomly chosen rope regions results in 0.15 pixel. The resulting mean parameter deviations are 0.32 mm for the strand lay length and 0.84 mm for the wire lay lengths. These small errors can be considered as a proof-of-concept for our deformation correction.

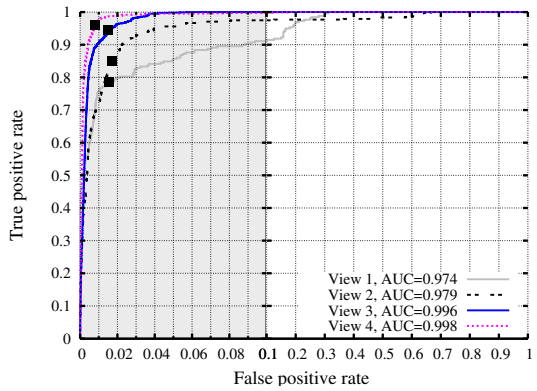

(a) Model-based approach.

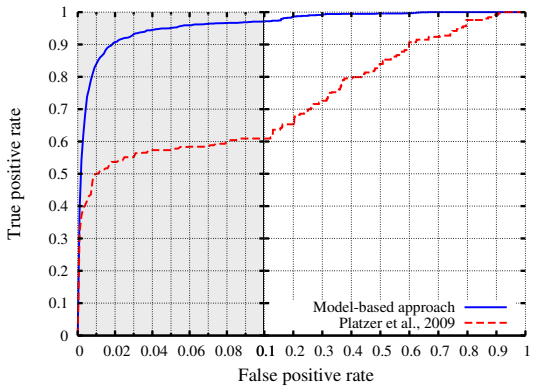

(b) Comparison of model-based approach and HMM-approach.

Figure 9: Quantitative evaluation of the model-based approach. In the left the ROC curves of the four camera views are shown. The 50% recovery-case is marked by the black squares. In the right the model-based approach is compared to the HMM-approach of Platzer et al. (2009) by means of averaged ROC curves.

6.4. Defect Detection Accuracy

The evaluation of the defect detection accuracy is exclusively performed on `RealRope`. We train the appearance model described in Section 4.2 for each camera view individually on 5 m of the rope, which the human expert considered to be defect free. The remaining 395 m were used for testing. The resulting ROC curves for each individual rope view can be seen in Figure 9(a). The AUC measure for each curve is given in the legend. The black squares mark the 50% recovery case. It becomes obvious, that the defection detection accuracy of our approach is very good. The worst-case FPR which must be tolerated to ensure that every defect is recognized to at least 50% lies around 1.5%. In most security relevant applications, the final decision must be made by a human expert who needs an image context of around 5 cm around each system alarm to judge weather it is a critical anomaly or a false alarm. Having regard to this circumstance, false alarm rate of 1.5% for the 50% defect recovery case imply that a human expert would have to re-inspect only 103 m of the rope instead of 395 m. The results illustrated in Figure 10 underline the good quality of our appearance model. In Figure 10(a)–10(d) some of our detection results are displayed. They emphasize the high accuracy of the anomaly detection as they almost perfectly match the defect region. Figure 10(e) and Figure 10(f) prove that the learned appearance representation is suitable for our purpose as the synthesized rope contains all important properties (reflections, shadowing etc.).

6.5. Comparison of the Defect Detection Accuracy with other Approaches

We compare our results to those obtained with the Hidden-Markov model (HMM) approach of Platzer et al. (2009) which leads to the best published results so far with regard to an individual analysis of each camera view. Figure 9(b) shows the averaged ROC curves (averaged over all four views) obtained on the same dataset with the HMM approach and with the model-based approach. It is obvious that our approach clearly outperforms the HMM-based strategy.

7. Conclusion

We argue that analyzing the rope surface with a model-based approach that incorporates the underlying structure of the rope is a great benefit compared to purely appearance-based approaches. By linking the observed appearance to the corresponding rope region, a much better representation of the normal surface characteristics can be obtained. Furthermore, the alignment of the 3d rope model with the 2d rope images allows the estimation of the current rope parameters and therefore a monitoring of the lay lengths within the rope. This is an important technical innovation, as an automatic measurement of these parameters was not possible before. The detection of creeping changes in the rope structure provides valuable information about the rope status. Finally, our experiments prove that the defect detection accuracy is improved significantly compared to the existing automatic approaches. The overall performance is comparable to the gold standard, which is up to now the human inspector.

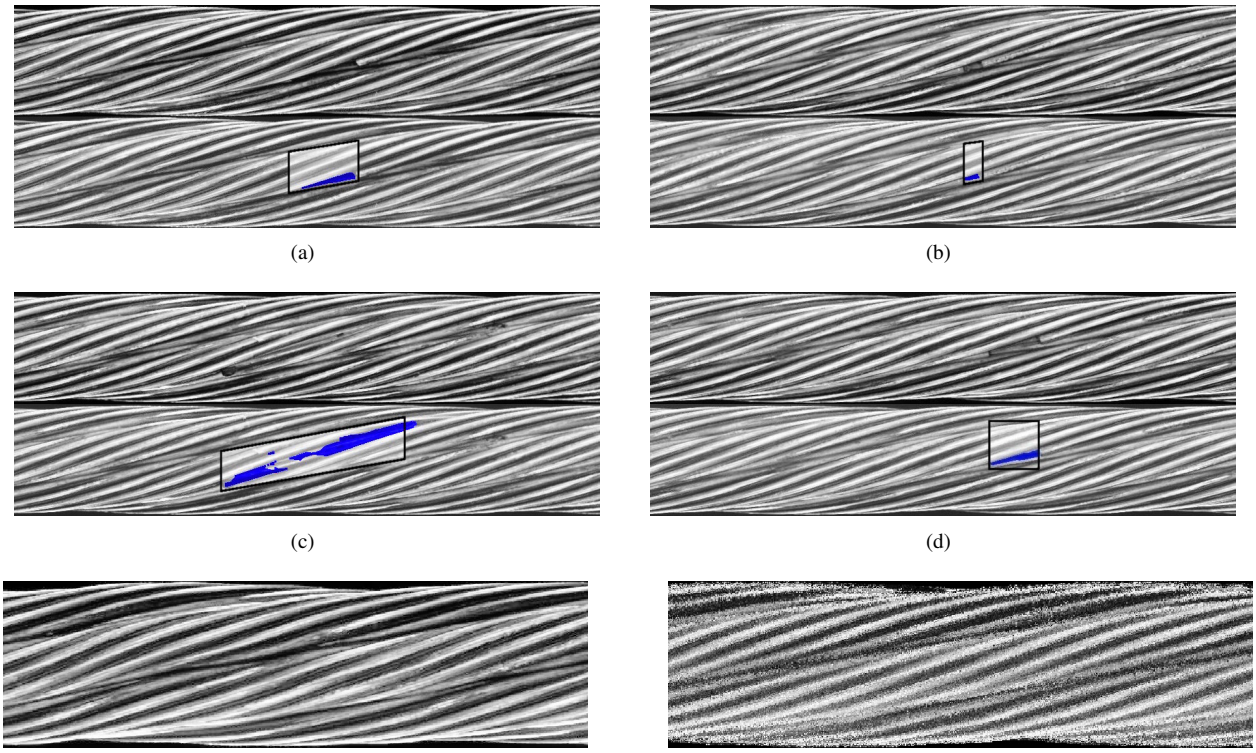

(a) (b) (c) (d) (e) Original rope image. (f) Artificially generated rope.

Figure 10: Recovered defects: original rope image (upper image in each group) and result with recovered defect (blue) and ground truth labeling (black box). (e) shows a part of real, intact rope and (f) shows an artificially generated rope projection, which was texturized with the learned model.

8. Further Work

Our approach is one of the first model-based approaches in this research area that incorporates structure and appearance. Thus, it would be interesting to apply the approach to other inspection problems. For arbitrary applications, the biggest part of the work would be the construction of a feasible, parametric 3d model. Despite its benefits our approach has still some drawbacks: the decision threshold which rules the classification rates is adapted manually at the moment. An automatic adaption could be a topic for further research. In addition, it would be interesting to replace the rigid rope model by a flexible one to reduce the systematic registration inaccuracies. However, a non-rigid registration would imply a new problem: a trade-off must be found between a good adaption to the intact rope on the one hand and too much adaption to abnormal rope deformations on the other hand. This implies an expansion of the classification problem by another dimension.

References

Chan, C., Pang, G. K. H., 2000. Fabric Defect Detection by Fourier Analysis. IEEE Transactions on Industry Applications 36 (5), 1267–1276.

Chandola, V., Banerjee, A., Kumar, V., 2009. Anomaly Detection: A Survey. ACM Computing Surveys 41 (3), 1–58.

Chetverikov, D., 2000. Structural Defects: General Approach and Application to Textile Inspection. In: Proceedings of the 15th International Conference on Pattern Recognition (ICPR). Vol. 1. pp. 521–524.

Chetverikov, D., Hanbury, A., 2002. Finding defects in texture using regularity and local orientation. Pattern Recognition 35 (10), 2165–2180.

Cohen, F., Tan, Z., Attali, S., 1991. Automated Inspection of Textile Fabrics using Textured Models. IEEE Transactions on Pattern Analysis and Machine Intelligence 8 (13), 803–808.

Dana, K. J., 2001. BRDF/BTF Mesurement Device. pp. 460–466.

Dana, K. J., van Ginneken, B., Nayar, S. K., Koenderink, J. J., 1999. Reflectance and Texture of Real-World Surfaces. ACM Transactions on Graphics 18 (1), 1–34.

Eisert, P., 2002. Model-based Camera Calibration Using Analysis by Synthesis Techniques. In: Greiner, G. (Ed.), Proceedings of the Vision, Modeling, and Visualization Conference (VMV 2002). Aka GmbH, pp. 307–314.

Feyrer, K., 2007. Wire ropes - Tension, Endurance, Reliablilty. Springer.

Gupta, R., Hartley, R., 1997. Linear Pushbroom Cameras. IEEE

Transactions on Pattern Analysis and Machine Intelligence 19 (9), 963–975.

Haase, D., Wacker, E.-S., Schukat-Talamazzini, E. G., Denzler, J., 2010. Analysis of Structural Dependencies for the Automatic Visual Inspection of Wire Ropes. In: Proceedings of the 15th International Workshop on Vision, Modelling, and Visualization (VMV 2010). pp. 49–56.

Hasler, N., Rosenhahn, B., Asbach, M., Ohm, J.-R., Seidel, H.-P., 2007. An Analysis-by-Synthesis Approach to Tracking of Textiles. In: Proceedings of the IEEE Workshop on Motion and Video Computing. p. 25.

Hodge, V., Austin, J., 2004. A Survey of Outlier Detection Methodologies. Artificial Intelligence Review 22 (2), 85–126.

Iivarinen, J., 2000. Surface Defect Detection with Histogram-Based Texture Features. In: Society of Photo-Optical Instrumentation Engineers (SPIE) Conference Series. Vol. 4197. pp. 140–145.

Jensen, H. W., 2001. Realistic Image Synthesis using Photon Mapping. A. K. Peters, Ltd. Natick, MA, USA.

Kajiya, J. T., 1986. The rendering equation. ACM SIGGRAPH Computer Graphics 20 (4), 143 – 150.

Koch, R., 1993. Dynamic 3D Scene Analysis through Synthesis Feedback Control. IEEE Transactions on Pattern Analysis and Machine Intelligence 15 (6), 556–568.

Koeser, K., Bartczak, B., Koch, R., 2007. An analysis-by-synthesis camera tracking approach based on free-form surfaces. In: Proceedings of the 29th DAGM Symposium on Pattern Recognition. LNCS. Springer, pp. 122–131.

Kumar, A., 2008. Computer-Vision-Based Fabric Defect Detection: A Survey. IEEE Transactions on Industrial Electronics 55 (1), 348–363.

Kumar, A., Pang, K. H., 2002. Defect Detection in Textured Materials Using Gabor Filters. IEEE Transactions on Industry Apllications 38 (2), 425–440.

Lafortune, E., 1996. Mathematical Models and Monte Carlo Alogrithms for Physically Based Rendering. Phd thesis.

Mäenpää, T., Turtinen, M., Pietikäinen, M., 2003. Real-time surface inspection by texture. Real-Time Imaging 9 (5), 289–296.

Mandriota, C., Stella, E., Nitti, M., Ancona, N., Distante, A., 2001. Rail corrugation detection by Gabor filtering. In: Proceedings of the IEEE International Conference on Image Processing (ICIP). Vol. 2. pp. 626–628.

Markou, M., Singh, S., 2003a. Novelty detection: a review - part 1: statistical approaches. Signal Processing 83 (12), 2481 – 2497.

Markou, M., Singh, S., 2003b. Novelty detection: a review - part 2: neural network bases approaches. Signal Processing 83 (12), 2499 – 2521.

Marschner, S. R., Westin, S. H., Lafortune, E. P. F., Torrance, K. E., 2000. Image-based Bidirectional Reflectance Distribution Function Measurement. Applied Optics 39 (16), 2592–2600.

McGill, R., Tukey, J., Larsen, W. A., 1978. Variations of Boxplots. The American Statistician 32, 12–16.

Moeslund, T. B., Hilton, A., Krüger, V., 2006. A survey of advances in vision-based human motion capture and analysis. Computer Vision and Image Understanding 104 (2), 90–126.

Moll, D., 2003. Innovative procedure for visual rope inspection. Lift Report 29 (3), 10–14.

Monadjemi, A., Mirmehdi, B., Thomas, B., 2004. Restructured Eigenfilter Matching for Novelty Detection in Random Textures. In: Proceedings of the 15th British Maschine Vision Conference (BMVC). pp. 637–646.

Niskanen, M., Silvén, O., Kauppinen, H., 2001. Color and Texture Based Wood Inspection with Non-supervised Clustering. In: Proceedings of the 12th Scandinavian Conference on Image Analysis (SCIA). pp. 336–342.

Penney, G. P., Weese, J., Little, J. A., Desmedt, P., Hill, D., Hawkes, D. J., 1998. A comparison of similarity measures for use in 2-d-3-d medical image registration. IEEE Transactions on Medical Imaging 17 (4), 586–595.

Phong, B., 1975. Illumination for Computer Generated Pictures. Communications of the ACM 18 (6), 311 – 317.

Platzer, E.-S., Nägele, J., Wehking, K.-H., Denzler, J., 2009. HMM-Based Defect Localization in Wire Ropes - A New Approach to Unusual Subsequence Recognition. In: Proceedings of the 31st Annual Symposium of the German Association for Pattern Recognition. pp. 442–451.

Platzer, E.-S., Süße, H., Nägele, J., Wehking, K.-H., Denzler, J., 2010. On the Suitability of Different Features for Anomaly Detection in Wire Ropes. In: et. al, A. R. (Ed.), Computer Vision, Imaging and Computer Graphics: Theory and Applications. Vol. 68. pp. 296–308.

Press, W., Teukolsky, S., Vetterling, W., Flannery, B., 1992. Numerical Recipes in C, 2nd Edition. Cambridge University Press, Cambridge, UK.

Provost, F. J., Fawcett, T., Kohavi, R., 1998. The Case against Accuracy Estimation for Comparing Induction Algorithms. pp. 445–453.

Rautkorpi, R., Iivarinen, J., 2005. Shape-Based Co-occurrence Matrices for Defect Classification. In: Proceedings of the 14th Scandinavian Conference on Image Analysis (SCIA). pp. 588–597.

Rodner, E., Wacker, E.-S., Kemmler, M., Denzler, J., 2011. One-Class Classification for Anomaly Detection in Wire Ropes with Gaussian Processes in a Few Lines of Code. In: Proceedings of the 12th IAPR Conference on Machine Vision Applications (MVA 2011). pp. 219–222.

Serdaroglu, A., Ertuzun, A., Ercil, A., 2006. Defect Detection in Textile Fabric Images Using Wavelet Transforms and Independent Component Analysis. Pattern Recognition and Image Analysis 16 (1), 61–64.

Shirley, P., 2002. Fundamentals of Computer Graphics. A. K. Peters, Ltd.

Tajeripour, F., Kabir, E., Sheikhi, A., 2008. Fabric Defect Detection Using Modified Local Binary Patterns. EURASIP Journal on Advances in Signal Processing 8 (1), 12 pages.

Tax, D. M. J., 2001. One-class classification - Concept-learning in the absence of counter-examples. Phd thesis, Technische Universitt Delft.

Tuceryan, M., Jain, A. K., 1998. The Handbook of Pattern Recognition and Computer Vision (2nd Edition). World Scientific Publishing Co., Ch. 2.1, pp. 207–248.

Unser, M., Ade, F., 1984. Feature extraction and decision procedure for automated inspection of textured materials. Pattern Recognition Letters 2 (3), 185–191.

Wacker, E.-S., Denzler, J., 2010. An Analysis-by-Synthesis Approach to Rope Condtion Monitoring. In: Proceedings of the 6th International Symposium on Visual Computing (ISVC). pp. 459–468.

Wuest, H., Wientapper, F., Stricker, D., 2007. Adaptable model-based tracking using analysis-by-synthesis techniques. In: Kropatsch, W., Kampel, M., Hanbury, A. (Eds.), In Proceedings of the 12th International Conference on Computer Analysis of Images and Patterns (CAIP). LNCS. Springer, pp. 20–27.

Xie, X., 2008. A Review of Recent Advances in Surface Defect Detection using Texture analysis Techniques. Electronic Letters on Computer Vision and Image Analysis 7 (3), 1–22.

Zhang, D. L., Cao, Y. N., Wang, C., Xu, D. G., 2006. A New Method of Defects Identification for Wire Rope Based on Three-Dimensional Magnetic Flux Leakage. Journal of Physics: Conference Series 48, 334–338.